Achieving true magnification in parallel ghost imaging at zero cost based on the cone beam characteristics of the X-ray tube

Nixi Zhao,[1,2,3] Junxiong Fang,[1,2,3] Jie Tang,[1,2,3] Changzhe Zhao,[1,2,3] Jianwen Wu,[1,2,3] Han Guo,[2] Haipeng Zhang,[2] and Tiqiao Xiao[1,2,3,*]

[1]Shanghai Institute of Applied Physics, Chinese Academy of Sciences, Shanghai 201800, People's Republic of China
[2]Shanghai Synchrotron Radiation Facility/Zhangjiang Lab, Shanghai Advanced Research Institute, Chinese Academy of Sciences, Shanghai 201204, People's Republic of China
[3]University of Chinese Academy of Sciences, Beijing 100049, People's Republic of China
[*]tqxiao@sari.ac.cn

Abstract: Ghost imaging (GI), as a novel imaging technique, facilitates image acquisition under low light conditions through single pixel measurements, thus holding great potential in various application areas ranging from biomedical imaging, remote sensing imaging, biometrics, astronomy to 3D imaging. However, to reconstruct high resolution images, GI typically requires a large number of single pixel samplings, which is extremely time consuming and poses practical limitations to its applications. Parallel ghost imaging treats each pixel of the position sensitive detector as a bucket detector and simultaneously performs tens of thousands of ghost imaging in parallel. In previous work, we gradually achieved parallel ghost imaging with high pixel resolution, low dose, and ultra large field of view. Parallel ghost imaging has demonstrated excellent performance and great potential. All this is so exciting. But since all our experiments were carried out at synchrotron radiation facilities, with a series of almost luxurious conditions such as nearly infinite and continuous light supply time, monochromatic, pure, and energy adjustable X rays, expensive and precise experimental equipment, and complete supporting facilities, many peers lacking experimental conditions cannot replicate parallel ghost imaging. Meanwhile, the high cost also hinders its cross field integration. Furthermore, we got rid of the synchrotron radiation source and completed the pipeline style acquisition of parallel ghost imaging in a way that uses rough and inexpensive equipment and is most imitable by others. We achieved high quality ghost imaging with an effective pixel size of 8.03 μm and an image size of 2880×2280 at a laboratory X ray source. The total cost of transforming an X ray computed tomography device into a parallel ghost imaging experimental platform is only $40. Parallel ghost imaging has been generalized from synchrotron radiation sources to X ray tubes.

However, a key problem remains unsolved. The object arm signal on our laboratory light source was obtained through artificial fitting, and the true magnification relationship between the reference arm and the object arm has not been established. In synchrotron radiation, we achieved true magnification using different magnifying optical lens groups. On the one hand, such a set of lenses is very expensive, making the generalization of parallel ghost imaging difficult again. On the other hand, the flux of the X ray tube is very small, which leads to extremely low efficiency. In this work, we find that compared with the parallel beam of synchrotron radiation, the cone beam of the X ray tube naturally has the characteristic of true magnification by gradually moving the detector away from the light outlet. We only use one detector. When collecting the object arm signal, the detector is moved to a position 30 cm away from the light outlet, and when collecting the reference arm signal, the detector is moved to a position 150 cm away from the light outlet. These two positions form a true magnification relationship of 5 times, achieving super resolution of parallel ghost imaging on the X ray tube. A series of high quality ghost imaging results with an effective pixel size of 7.095 μm and an image size of 2880×2280 in pipeline style acquisition were obtained. The realization of true magnification based on the X ray tube is a prerequisite

for achieving ultra large field of view and low dose imaging. Completing this work at zero cost implies great application value and commercial potential.

1. Introduction

The traditional imaging model primarily consists of three components: the light source, the object, and the optical system. In contrast, ghost imaging (GI), a novel imaging technique, employs a non-localized approach to separate detection from imaging. Ghost imaging involves splitting the light into two beams: one beam carries the object information but lacks resolution, while the other beam carries resolution but lacks object information. Neither beam alone is capable of imaging, but by correlating the two beams computationally, the object information can be reconstructed. Hence, ghost imaging is also referred to as correlation imaging.

Ghost imaging originates from the Hanbury-Brown and Twiss (HBT) experiment [1, 2]. In 1988, Klyshko [3] theoretically proposed a ghost imaging scheme using entangled photon pairs. In 1994, Ribeiro et al. [4] discovered the phenomenon of ghost interference using entangled photon pairs. In 1995, Pittman et al. [5] experimentally demonstrated ghost imaging using entangled photon pairs. In 2002, Bennink et al. [6] realized ghost imaging with classical light sources, proving that entangled light sources are not a necessary condition for ghost imaging. Furthermore, ghost imaging has been shown to be feasible in various fields, including atomic [7], electronic [8], neutron [9, 10], and X-ray [11–15] imaging. In 2008, Shapiro [16] theoretically proposed a computational ghost imaging scheme, making single-channel ghost imaging possible. In 2009, Bromberg et al. [17] experimentally realized computational ghost imaging. In the same year, Katz et al. [18] integrated compressive sensing techniques from image processing with computational ghost imaging, significantly reducing the number of samples required for ghost imaging. This development made dose reduction in X-ray ghost imaging feasible. Moreover, ghost imaging has enormous potential across various application areas, including biomedical imaging [19], remote sensing [20], biometrics [21, 22], astronomy [23], and three-dimensional imaging [24, 25].

However, to reconstruct high-resolution images, Ghost imaging typically requires a large number of single-pixel samples, which poses challenges for its practical application. The concept of parallel ghost imaging (PGI) was introduced by Kingston et al. [9] to address this issue. This method treats each pixel of a position-sensitive detector as an independent bucket detector, enabling the simultaneous execution of tens of thousands of ghost imaging measurements at once. Kingston et al. and Zhang et al. successfully demonstrated PGI in neutron [9] and X-ray [26, 27], respectively. O. Sefi et al. customized a gold mask with extremely high aspect ratio structures through X-ray lithography technology, making high-energy X-ray parallel ghost imaging possible. Moreover, they combined parallel ghost imaging with CT to achieve parallel ghost tomography [28].

In our previous work, we established a true magnification configuration between the reference arm and the object arm using lenses, achieving high-pixel-resolution parallel imaging at the sub-micron level (0.325 µm/pixel) and increasing the experimental efficiency from dozens of minutes to just a few minutes [29]. Zhao et al. achieved low-dose ghost imaging by using two detectors in crystal-splitting ghost imaging. By constructing an extra-large speckle space, we realized ghost imaging with an extra-large field of view of 14000×10000 pixels [30]. We also specifically proposed global ghost imaging for the bucket detector array architecture, which can achieve high-quality reconstruction with an ultra-low sampling rate of only 8 measurements. Moreover, this method can eliminate the discontinuity between ghost imaging subsystems [31]. Subsequently, we replaced the crystal splitting with a computational ghost imaging framework to achieve low-dose ghost imaging, significantly improving the image quality and, for the first time, simultaneously realizing large-field-of-view, low-dose, and high-pixel-resolution ghost imaging [32].

However, the transformation of scientific research achievements has run into difficulties. All the above progress was completed relying on the Shanghai Synchrotron Radiation Facility. The nearly infinite and continuous light supply time, monochromatic, pure, and energy-adjustable X-rays, expensive and precise experimental equipment, and the complete supporting facilities – this series of almost luxurious services provided by synchrotron radiation make it impossible for many peers lacking experimental conditions to replicate parallel ghost imaging. At the same time, the high cost has also hindered its cross-disciplinary integration.

We got rid of the synchrotron radiation source and completed the pipeline-style collection of parallel ghost imaging with rough and inexpensive equipment in the most imitable way. Eventually, with a laboratory X-ray source, we achieved ghost imaging with an effective pixel size of 8.03 µm, an image size of 2880×2280, and a minimum of 10 measurement numbers (a sampling rate of 0.62%) [33].

However, a key problem still remains unsolved. The object arm signal in our laboratory light source was obtained through artificial fitting, and the true magnification relationship between the reference arm and the object arm has not been established yet. In synchrotron radiation, we achieved true magnification using different magnification optical lens sets [29]. On one hand, such a set of lenses is very expensive, making the generalization of parallel ghost imaging difficult again. On the other hand, the flux of the X ray tube is very small, and adding an optical lens set in the light path will further reduce the flux, resulting in extremely low efficiency.

In this work, we find that compared with the parallel beam of synchrotron radiation, the cone beam of the X ray tube naturally has the characteristic of true magnification by gradually moving the detector away from the light outlet. When collecting the object arm data, the detector is moved to a position 30 cm away from the light outlet, and when collecting the reference arm data, the detector is moved to a position 150 cm away from the light outlet. These two positions form a true magnification relationship of 5 times. We used only one detector and achieved super resolution of parallel ghost imaging with the X ray tube without incurring any additional costs. A series of high quality ghost imaging results with an effective pixel size of 7.095 µm and an image size of 2880×2280 were obtained through pipeline style acquisition. The realization of true magnification based on the X ray tube is a prerequisite for achieving ultra large field of view and low dose imaging. Completing this work at zero cost implies great application value and commercial potential, and will further accelerate the generalization of parallel ghost imaging in various fields. Parallel ghost imaging exhibits unique advantages with its non local imaging feature, such as low dose and low cost, and is expected to challenge traditional projection imaging.

2. Methods and experiments

Model For the ghost imaging model from a classical perspective, the bucket detector signals acquired from N measurements in object arm can be written in the form of a matrix in Eq.1.

$$\begin{bmatrix} B_1 \\ B_2 \\ \vdots \\ B_N \end{bmatrix} = \begin{bmatrix} I_1(1,1) & I_1(1,2) & \cdots & I_1(p,1) & \cdots & I_1(p,q) \\ I_2(1,1) & I_2(1,2) & \cdots & I_2(p,1) & \cdots & I_2(p,q) \\ \vdots & \vdots & \vdots & \vdots & \vdots & \vdots \\ I_N(1,1) & I_N(1,2) & \cdots & I_N(p,1) & \cdots & I_N(p,q) \end{bmatrix} \begin{bmatrix} T(1,1) \\ T(1,2) \\ \vdots \\ T(p,q) \end{bmatrix} \tag{1}$$

The object's transmittance function $T(x, y)$, which contains internal structural information of the sample, is the unknown target we aim to reconstruct in ghost imaging. Both the image size of the mask and the reconstructed ghost image of samples are $p \times q$. The transmittance function of the k-th mask is denoted as $I_k(x, y)$, where $x = 1, \cdots, p$ and $y = 1, \cdots, q$, respectively.

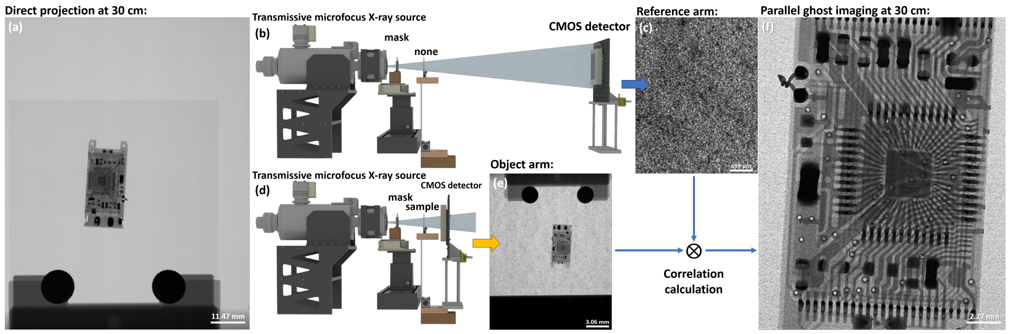

Fig. 1. Experimental schematic diagram of true magnification parallel ghost imaging based on the cone beam characteristics of the X-ray tube. (b) Schematic diagram of the reference arm. (c) The speckle pattern collected in the reference arm, which contains no sample information but has high resolution. (d) Schematic diagram of the object arm. (e) The signal of the array bucket detector collected in the object arm, which contains sample information but has low resolution. When directly using traditional direct projection imaging, the imaging result is shown in (a). In contrast, if parallel ghost imaging is used, the imaging result is super-resolved and magnified as shown in (f).

N represents the number of measurements, B_i denotes the bucket detector signal during the i-th measurement, and the sampling rate is defined as the number of measurements divided by the number of image pixels, i.e. $\frac{N}{p \times q}$. A higher sampling rate leads to higher quality of ghost imaging. For the detector in the object arm, the incident X-ray photons need to pass through the mask and subsequently through the object, which means that the absorption of both the mask and object should be taken into account. Ghost imaging, at its essence, is solving underdetermined linear equation set. PGI simply utilizes this process repeatedly for all the single pixels of the bucket detector array in the object arm.

Algorithm PGI is based on the Total Variation Augmented Lagrangian Alternating Direction Algorithm [34] using compressive sensing. TVAL3 uses Total Variation Regularization (TV) as an iterative model:

$$\underset{u}{min} \sum_i \|D_i u\|, \quad s.t. Au = b, \tag{2}$$

A is the speckle patterns, u is the image of the object to be solved, b is the measurements of the bucket detector, $D_i u$ is the gradient of u at pixel i, $\|.\|$ is the $l1$ norm. The Augmented Lagrangian method transforms a constrained model into an unconstrained objective function, and then uses the Alternating Direction method to solve the objective function at high speed.

Experiment In our previous work, we were able to modify any experimental platform capable of implementing computed tomography to achieve X-ray parallel ghost imaging. This only requires an extremely low cost of $40 and is very easy for others to replicate. In this experiment, the laboratory light source used is the microfocus X-ray source (XWT-225 The Plus) from X-RAY WorX. It has a maximum voltage of 225 kV, a minimum voltage of 20 kV, a current ranging from 0.05 mA to 1 mA, a maximum emission power of 80 W, and a maximum target power of 50 W. It belongs to a transmission-type X-ray tube, with the target material composed of diamond and tungsten. The radiation angle is 160°, and the resolution can reach the sub-micron level. The detector used is a CMOS camera (Teledyne DALSA Shad-o-Box 6K HS), with a pixel number of 2940 × 2304, an effective area of 14.6 cm × 11.4 cm, and a resolution of 49.5 µm.

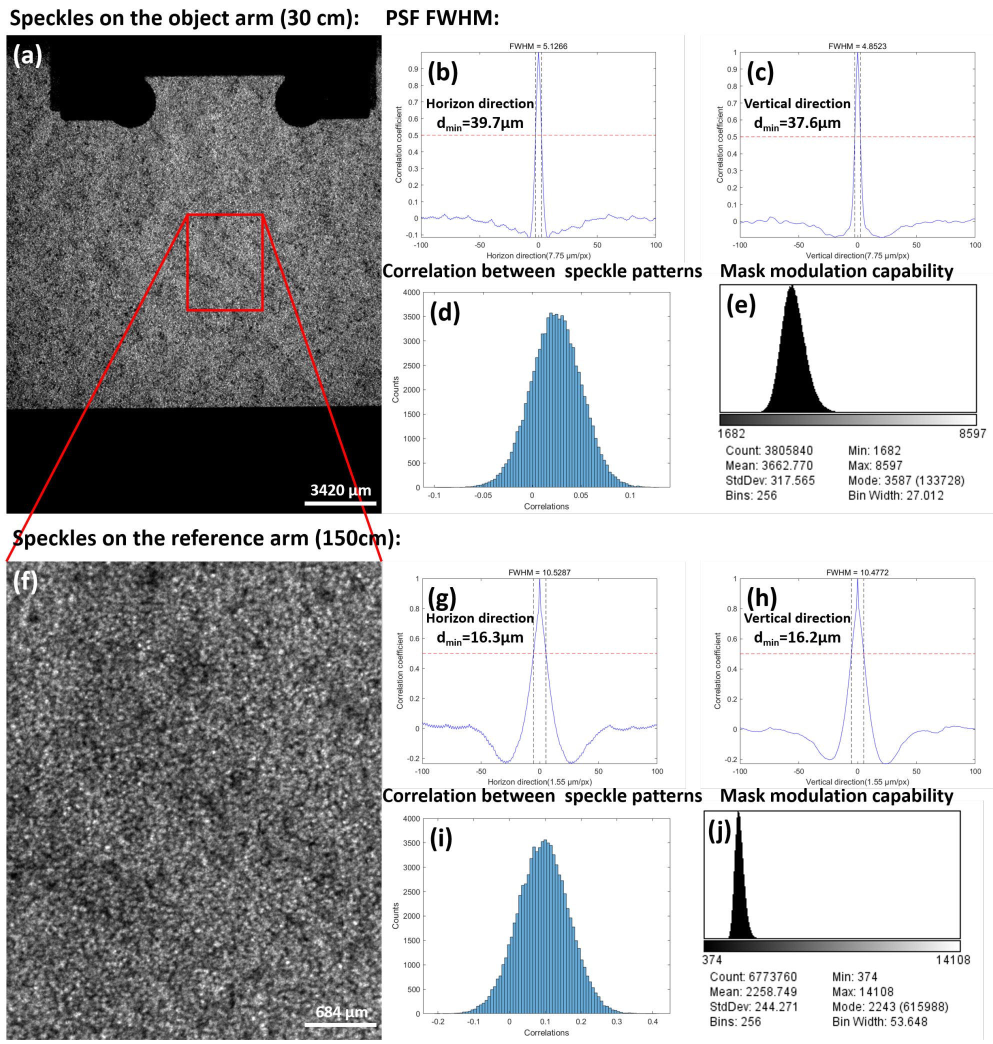

Fig. 2. Speckle analysis. True magnification leads to an improvement in the resolution of the minimum effective characteristics of the speckles. (a) The speckle pattern collected in the object arm. The full width at half maximum (FWHM) of its point spread function (PSF) in the horizontal direction is shown in (b) and in the vertical direction is shown in (c). (f) The speckle pattern collected in the reference arm. The full width at half maximum (FWHM) of its point spread function (PSF) in the horizontal direction is shown in (g) and in the vertical direction is shown in (h). By comparison, it can be seen that the resolution of the minimum effective characteristics has been improved by more than twice. The correlation degree between the speckles is shown in (d) for the object arm and (i) for the reference arm. The modulation ability of the mask is shown in (e) for the object arm and (j) for the reference arm.

The total cost of modifying the CT experimental platform is $40, which is exactly the price of the copper foam and sandpaper used to modulate the light field. From the perspective of commercial production, the experiment should minimize costs as much as possible while achieving the highest possible image quality. In this work, we will continue to adhere to this concept. We will achieve true magnification between the reference arm and the object arm without incurring any additional costs. Precise movement of the mask is necessary in each measurement, and it is achieved by placing the mask on the sample stage of the CT X-ray machine. True magnification requires that the mask, the sample, and the detector of the object arm be as close as possible to the light outlet. Therefore, the motor complex carrying the mask should be as close as possible to the light outlet, and at the same time, the detector of the object arm should be as close as possible to the mask. Due to the safety distance limiting device between the equipment, a distance of more than ten centimeters will be reserved between the mask and the detector. Our sample stage is placed in this gap. The distances from the mask, the sample, and the detector to the light outlet are utilized without any waste, which is a necessary condition for achieving true magnification parallel ghost imaging in the X-ray tube, as shown in Fig.5.(f). This involves a unique discussion of parallel ghost imaging under the condition of a cone beam. The magnification factor of true magnification and the effective size of the speckles are related to the distances from the mask, the sample, the detector of the object arm, and the detector of the reference arm to the light outlet. We will elaborate on this later.

The detector of the reference arm is placed at a distance of 150 cm from the light outlet, and the optical path of the reference arm is shown in Fig.1.(b). At this time, the sample stage is empty, and the collected high-resolution speckle pattern is shown in Fig.1.(c). The detector of the object arm is placed at a distance of 30 cm from the light outlet, and the optical path of the object arm is shown in Fig.1.(d). The signal of the bucket detector array collected by the detector of the object arm is shown in Fig.1.(e). If the mask is not placed, the result of traditional projection imaging achieved by the detector at a distance of 30 cm is shown in Fig.1.(a). Parallel ghost imaging non-locally correlates and calculates the object arm signal with object information but low resolution and the reference arm signal without object information but high resolution. It can reconstruct the effect that traditional imaging can only achieve at a detection distance of 150 cm at a detection distance of 30 cm. The reconstruction result of parallel ghost imaging is shown in Fig.1.(f). The intuitive comparison between Fig.1.(e) and (f) proves that we have achieved super-resolution on the X-ray tube.

Super resolution Whether super-resolution has truly been achieved still requires a series of substantial evidences. The mask is placed at a distance of 4.7 cm from the light outlet, and the pixel size of the detector is 49.5 μm. Due to the magnification effect of the cone beam, the equivalent pixel sizes of the mask at the object arm (30 cm) and the reference arm (150 cm) are 7.75 μm and 1.55 μm respectively, as evidenced in Fig.5.(a) and (b). The effective pixel size of the reference arm is five times that of the object arm. This evidence is necessary but not sufficient. This is because the effective aperture size of the speckles may not increase proportionally with the improvement of the pixel resolution, and the effective aperture size of the speckles determines the theoretical upper limit of the resolution of the ghost imaging reconstruction results. Therefore, a series of discussions on the effective aperture size of the speckles will be presented below.

In the experiment, the voltage of the microfocus X-ray tube is 70 kV and the current is 120 mA. This implies that the output X-ray energy spectrum is a continuous spectrum that includes the characteristic peak of tungsten and has a maximum electron energy of 70 keV. The photon energy of the X-ray tube is much higher than that of synchrotron radiation, and photons with different energies pose difficulties for the modulation of the light field. The discussions and analyses regarding the interaction between the mask and photons with different energies have

been provided in our work on the generalization of parallel ghost imaging [33]. Therefore, we continue to adopt the mixed mask strategy consisting of 4 layers of 200-mesh sandpaper, a dense copper foam with a thickness of 0.2 mm and an aperture of 10 μm, and 3 layers of 200-mesh sandpaper. When no sample is placed, the speckle pattern collected by the object arm is shown in Fig.2.(a). The full width at half maximum (FWHM) of the point spread function (PSF) can provide the minimum effective characteristic size of the speckle pattern of the object arm, which is 39.7 μm in the horizontal direction and 37.6 μm in the vertical direction, as shown in Fig.2.(b) and (c). Similarly, the minimum effective characteristic size of the speckle pattern collected by the reference arm is 16.3 μm in the horizontal direction and 16.2 μm in the vertical direction, as shown in Fig.2.(g) and (h). By comparison, it can be seen that the minimum effective resolution provided by the reference arm is approximately 2.4 times that of the object arm, indicating that the conditions for achieving super-resolution in ghost imaging are met. To avoid ineffective measurements in ghost imaging, we need the random speckles to be as dissimilar as possible. The low correlation degree between the speckle patterns demonstrates that the random speckles can be approximately regarded as orthogonal to each other, as shown in Fig.2.(d) and (l). The modulation ability of the mask is shown in Fig.2.(e) and (j).

3. Results and true amplification

Results From the perspectives of industrialization and commercialization, it is essential to efficiently complete the measurement of a series of samples. Before parallel ghost imaging could be separated from synchrotron radiation, we had already achieved pipelined sample collection. For the collection of the object arm for a series of samples, it is only necessary to pre-record a set of the reference arm. The exposure time for measuring the reference arm is 8 seconds, and the exposure time for measuring the object arm is 0.1 seconds. We simulated the scenario of factory pipeline collection with a set of chips (small chip, medium chip, and large chip). The actual pictures of the three chips are shown in Fig.5.(l), and their traditional direct projection images at a distance of 30 cm are shown in Fig.5.(i), (j), and (k).

Finally, we reconstructed a series of results with an image size of 2880×2280 and an equivalent pixel size of 7.095 μm in a pipelined manner. Each pixel of the detector of the object arm corresponds to a 5×5 pixel block of the reference arm, and the results with different numbers of measurements/sampling rates are displayed in Fig.3. The traditional direct projection images of the chips at a distance of 150 cm are listed in Fig.3 and 4.(a), (l), and (w) and are listed on the far left as the reference standard. After achieving true magnification, the experimental results demonstrate astonishing image quality while maintaining a large field of view and high pixel resolution. We confidently claim that such high-quality results are the first in the world in the field of X-ray ghost imaging. Structural similarity (SSIM) is an index that can effectively measure the similarity between the results of parallel ghost imaging and the reference standard. The SSIM curve with the number of measurements ranging from 2 to 400 is shown in Fig.5.(g). This provides strong evidence for our assertion.

We believe that it is necessary to conduct further exploration to verify the reliability of the method. Firstly, due to the fact that the radiation protection shell of the CT platform is not large enough, the detector of the reference arm cannot be further away from the light outlet, and a true magnification of 5 times is already the limit. Secondly, in our previous study on the influence of the block size on the reconstruction quality [26], we found that a pixel block of 40×40 is the optimal choice. Thirdly, to achieve true magnification in the reference arm and the object arm, registration is a key issue. A 5×5 pixel block is too small to distinguish the alignment effect. Therefore, on the basis of a true magnification of 5 times, we further fit an 8×8 artificially fitted detector into a bucket detector to form a magnification correspondence of 40×40 times to explore the reliability of the imaging results. A series of results with different numbers of measurements/sampling rates for pixel blocks of 40×40 in size are displayed in Fig.4. Larger

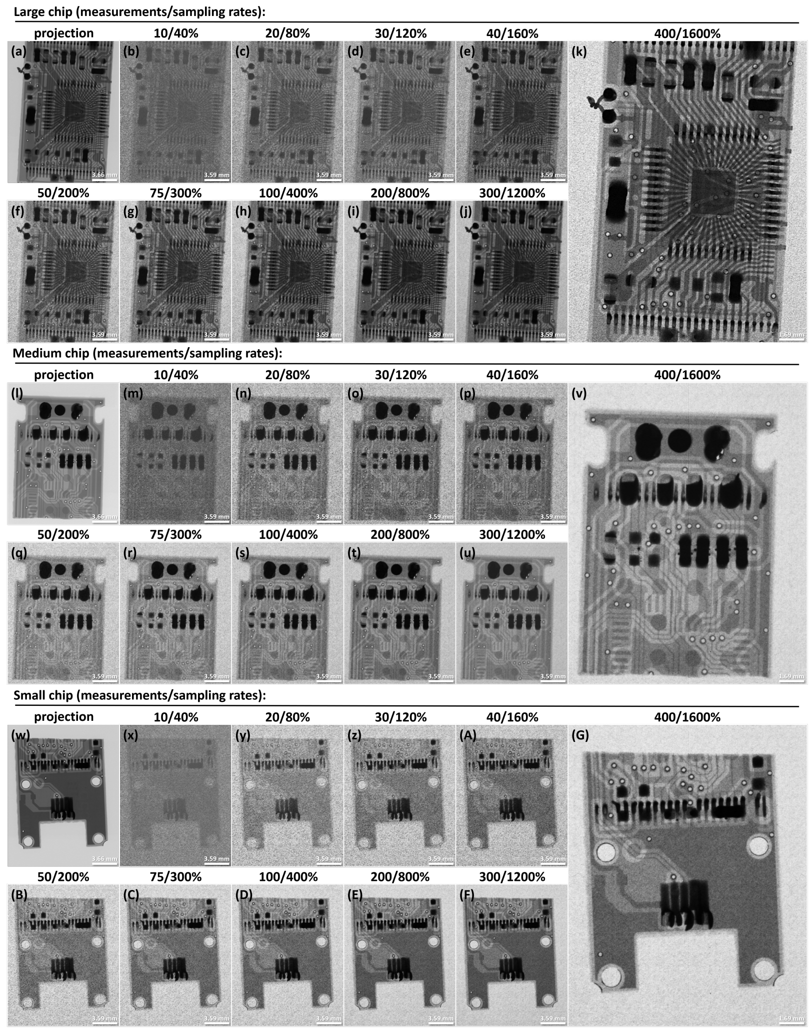

Fig. 3. The imaging results with a true magnification of 5 times. For the large-sized chip sample: (a), as the standard reference, is the projection imaging at a distance of 150 cm. The correspondence between the number of measurements/sampling rate and the results is as follows: (b) 10/40%, (c) 20/80%, (d) 30/120%, (e) 40/160%, (f) 50/200%, (g) 75/300%, (h) 100/400%, (i) 200/800%, (j) 300/1200%, (k) 400/1600%. For the medium-sized chip sample: (l), as the standard reference, is the projection imaging at a distance of 150 cm. The correspondence between the number of measurements/sampling rate and the results is as follows: (m) 10/40%, (n) 20/80%, (o) 30/120%, (p) 40/160%, (q) 50/200%, (r) 75/300%, (s) 100/400%, (t) 200/800%, (u) 300/1200%, (v) 400/1600%. For the small-sized chip sample: (w), as the standard reference, is the projection imaging at a distance of 150 cm. The correspondence between the number of measurements/sampling rate and the results is as follows: (x) 10/40%, (y) 20/80%, (z) 30/120%, (A) 40/160%, (B) 50/200%, (C) 75/300%, (D) 100/400%, (E) 200/800%, (F) 300/1200%, (G) 400/1600%.

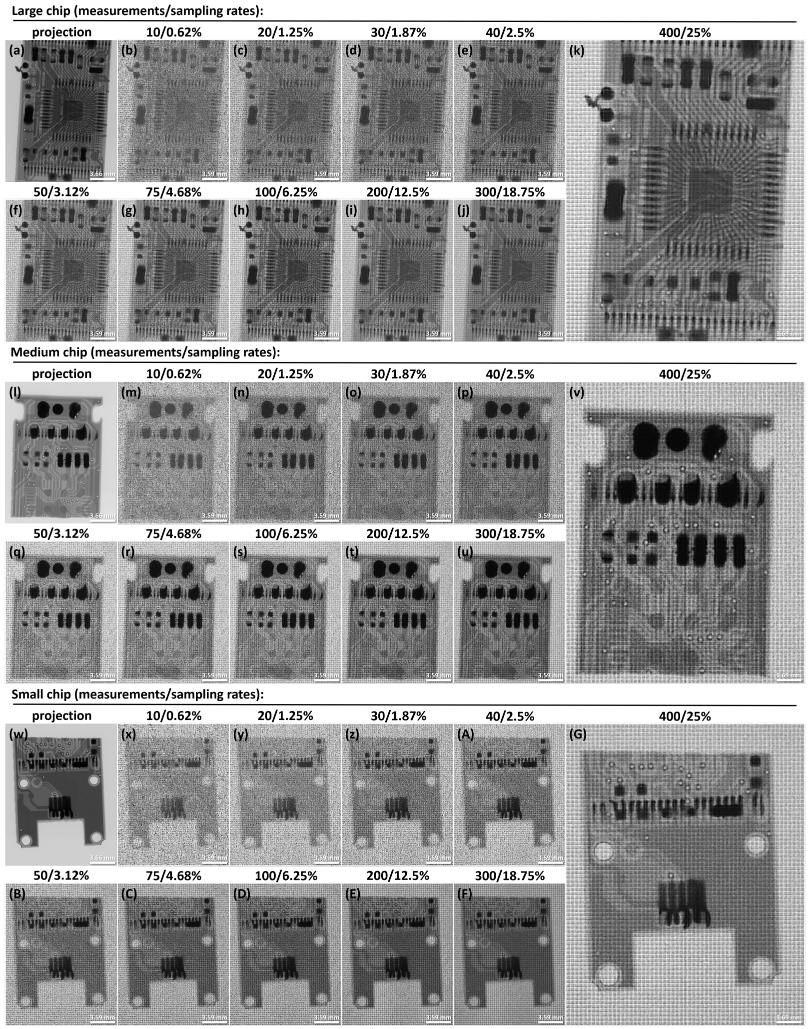

Fig. 4. The imaging results with a true magnification of 5 times and an artificially fitted magnification of 8 times. For the large-sized chip sample: (a), as the standard reference, is the projection imaging at a distance of 150 cm. The correspondence between the number of measurements/sampling rate and the results is as follows: (b) 10/0.62%, (c) 20/1.25%, (d) 30/1.87%, (e) 40/2.5%, (f) 50/3.12%, (g) 75/4.68%, (h) 100/6.25%, (i) 200/12.5%, (j) 300/18.75%, (k) 400/25%. For the medium-sized chip sample: (l), as the standard reference, is the projection imaging at a distance of 150 cm. The correspondence between the number of measurements/sampling rate and the results is as follows: (m) 10/0.62%, (n) 20/1.25%, (o) 30/1.87%, (p) 40/2.5%, (q) 50/3.12%, (r) 75/4.68%, (s) 100/6.25%, (t) 200/12.5%, (u) 300/18.75%, (v) 400/25%. For the small-sized chip sample: (w), as the standard reference, is the projection imaging at a distance of 150 cm. The correspondence between the number of measurements/sampling rate and the results is as follows: (x) 10/0.62%, (y) 20/1.25%, (z) 30/1.87%, (A) 40/2.5%, (B) 50/3.12%, (C) 75/4.68%, (D) 100/6.25%, (E) 200/12.5%, (F) 300/18.75%, (G) 400/25%.

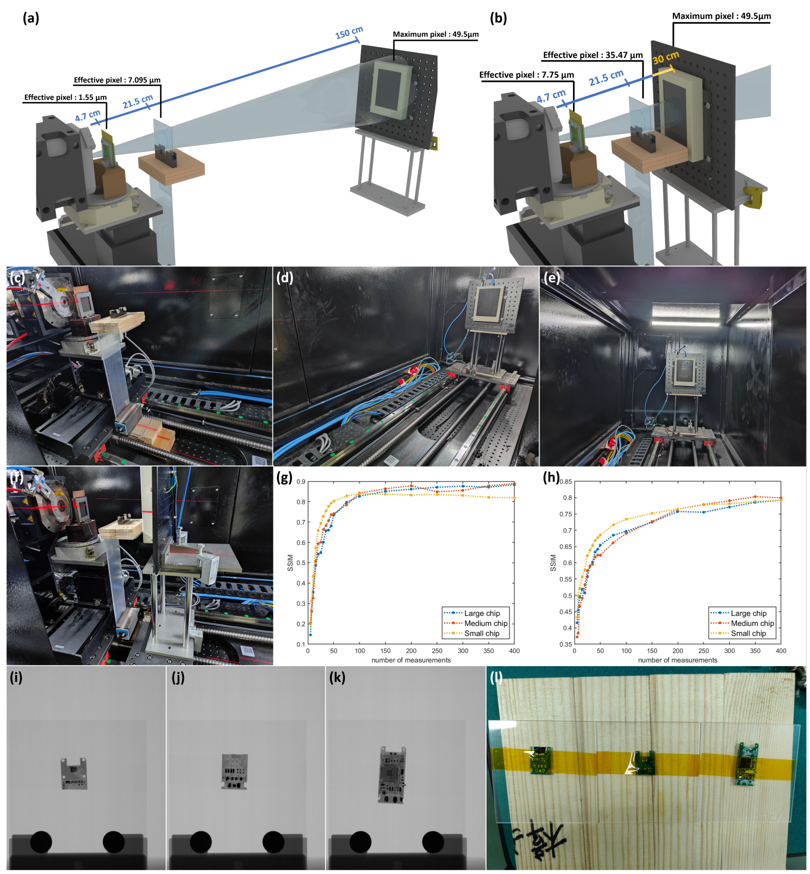

Fig. 5. (a) The effective resolution of the mask and the sample in the reference arm. (a) The effective resolution of the mask and the sample in the object arm. To achieve a higher true magnification, the detector of the reference arm should be placed as far away as possible from the light outlet, and the physical diagrams of the reference arm device can be seen in (c), (d) and (e). A more effective way to increase the magnification is to make the detector of the object arm as close as possible to the light outlet, and the physical diagram of the object arm device can be seen in (f). (g) The structural similarity (SSIM) curve diagrams comparing the small chip, the medium chip and the large chip with different sampling rates and their direct projection under a true magnification of 5 times. (h) The structural similarity curve diagrams comparing the small chip, the medium chip and the large chip with different sampling rates and their direct projection under a true magnification of 5 times and then an artificial fitting magnification of 8 times. (i) The direct projection diagram of the small chip at a distance of 30 cm. (j) The direct projection diagram of the medium chip at a distance of 30 cm. (k) The direct projection diagram of the large chip at a distance of 30 cm. (l) The physical diagrams of the chips.

pixel blocks mean a lower sampling rate, poorer image quality, and a lower dose under the same number of measurements. Although the image quality has decreased, the image reconstruction proves that we have indeed achieved the registration of the reference arm and the object arm at zero cost. The SSIM curve is shown in Fig.5.(h).

True magnification In our previous work, we achieved the generalization of parallel ghost imaging for X-ray tube. However, the bucket detector array of the object arm was artificially fitted, and we failed to successfully establish a true magnification relationship between the object arm and the reference arm. This means that the super-resolution characteristic of ghost imaging was not realized, and thus the low-dose and large field of view that rely on super-resolution could not be achieved either. In this work, we utilized the cone beam characteristics of the X-ray tube to achieve true magnification, solving the core problem of parallel ghost imaging with an X-ray tube. Some phenomena related to true magnification did not occur in previous work, and it is necessary to discuss them separately.

The mask is 4.7 cm away from the light outlet, the sample is 21.5 cm away from the light outlet, the detector of the reference arm is 150 cm away from the light outlet, and the detector of the object arm is 30 cm away from the light outlet. The device diagrams of the reference arm are shown in Fig.5.(c), (d), and (e), and those of the object arm are shown in Fig.5.(f). In the object arm, the effective resolutions of the mask and the sample are 7.75 μm and 35.47 μm respectively, as shown in Fig.5.(b). In the reference arm, the effective resolutions of the mask and the sample are 1.55 μm and 7.095 μm respectively, as shown in Fig.5.(a). We found that the effective resolution of the speckle pattern is decoupled from the effective resolution of the sample, which is quite different from parallel ghost imaging with synchrotron radiation and parallel ghost imaging with an X-ray tube without achieving true magnification. The effective pixel size of the speckles in parallel ghost imaging is 1.55 μm, while the effective pixel size of the sample is 7.095 μm, and we have indicated this in the scale bars of Fig.2.(f) and Fig.3 or 4. In parallel ghost imaging with cone beam magnification, the magnification factors of the mask and the sample have nothing to do with their distances from the light outlet, and are only related to the ratio of the distances of the detectors in the object arm and the reference arm. A higher magnification factor requires the detector of the reference arm to be as far away from the light outlet as possible, but this is not as easy to achieve as making the detector of the object arm as close to the light outlet as possible. Moving the detector of the reference arm several meters further away from the light outlet achieves the same magnification factor as moving the detector of the object arm several centimeters closer to the light outlet, which means that the crowded optical path of the object arm is more cost-effective. The cone beam magnification also enlarges the size of the speckles. On the one hand, this requires the mask to have smaller aperture characteristics. On the other hand, perhaps the structure with the sample in front and the mask behind is more reasonable.

4. Conclusion

In conclusion, in our previous work, we successfully achieved the three key characteristics of parallel ghost imaging, namely high pixel resolution, ultra-large field of view, and low dose, respectively, through the use of synchrotron radiation. Additionally, we specifically proposed global ghost imaging for the architecture of the bucket detector array to eliminate the discontinuities between blocks. The parallel ghost imaging framework has been demonstrated to possess immense application potential and commercial value. We accomplished the transformation from a CT X-ray machine to a parallel ghost imaging experimental platform at a minimum cost of only 40 US dollars and via the approach that is most accessible for our peers to replicate. In this current work, the significant problem of the inability to achieve true magnification in parallel ghost imaging using an X-ray tube has been resolved at no cost. This signifies that ghost imaging has

taken another crucial step forward on the path towards practical application and commercialization.

Although this work has addressed the core issue existing in parallel ghost imaging with an X-ray tube, it still falls far short of our expectations. A true magnification ratio of 40 times is what we are striving for. Parallel ghost imaging is required to reconstruct sample details that traditional imaging methods cannot capture, and the disparity between the two should be large enough to be discernible with the naked eye. In other words, achieving a sample effective resolution that is significantly higher than the current level is a rigid criterion for parallel ghost imaging to replace traditional imaging. This core challenge is the only obstacle hindering parallel ghost imaging from achieving industrialization. If it can be overcome, it implies that parallel ghost imaging will have a profound impact on the field of medical imaging.

Funding. The National Key Research and Development Program of China (Grant Nos. 2022YFA1603601, 2021YFF0601203, 2021YFA1600703), the Young Scientists Fund of the National Natural Science Foundation of China (Grant No.12205361)

Acknowledgment. The authors thank WenJie Hao, Kang Du, Zenghao Song, JunXiong Fang, YanLing Xue, Ke Li and FeiXiang Wang for their kind help and fruitful discussion on experiments and data processing.

Disclosures. The authors declare no conflicts of interest.

Data Availability Statement. Data underlying the results presented in this paper are not publicly available at this time but may be obtained from the authors upon reasonable request.

References

1. R. Hanbury Brown and R. Q. Twiss, "A test of a new type of stellar interferometer on sirius," in *A Source Book in Astronomy and Astrophysics, 1900–1975,* (Harvard University Press, 1979), pp. 8–12.
2. R. H. Brown and R. Q. Twiss, "Correlation between photons in two coherent beams of light," Nature **177**, 27–29 (1956).
3. D. Klyshko, "Two-photon light: influence of filtration and a new possible epr experiment," Phys. Lett. A **128**, 133–137 (1988).
4. P. S. Ribeiro, S. Pádua, J. M. Da Silva, and G. Barbosa, "Controlling the degree of visibility of young's fringes with photon coincidence measurements," Phys. Rev. A **49**, 4176 (1994).
5. T. B. Pittman, Y. Shih, D. Strekalov, and A. V. Sergienko, "Optical imaging by means of two-photon quantum entanglement," Phys. Rev. A **52**, R3429 (1995).
6. R. S. Bennink, S. J. Bentley, and R. W. Boyd, ""two-photon" coincidence imaging with a classical source," Phys. review letters **89**, 113601 (2002).
7. R. I. Khakimov, B. Henson, D. Shin, *et al.*, "Ghost imaging with atoms," Nature **540**, 100–103 (2016).
8. S. Li, F. Cropp, K. Kabra, *et al.*, "Electron ghost imaging," Phys. review letters **121**, 114801 (2018).
9. A. M. Kingston, G. R. Myers, D. Pelliccia, *et al.*, "Neutron ghost imaging," Phys. Rev. A **101**, 053844 (2020).
10. Y.-H. He, Y.-Y. Huang, Z.-R. Zeng, *et al.*, "Single-pixel imaging with neutrons," Sci. Bull. **66**, 133–138 (2021).
11. H. Yu, R. Lu, S. Han, *et al.*, "Fourier-transform ghost imaging with hard x rays," Phys. review letters **117**, 113901 (2016).
12. D. Pelliccia, A. Rack, M. Scheel, *et al.*, "Experimental x-ray ghost imaging," Phys. review letters **117**, 113902 (2016).
13. A. Schori and S. Shwartz, "X-ray ghost imaging with a laboratory source," Opt. express **25**, 14822–14828 (2017).
14. D. Pelliccia, M. P. Olbinado, A. Rack, *et al.*, "Towards a practical implementation of x-ray ghost imaging with synchrotron light," IUCrJ **5**, 428–438 (2018).
15. A. Schori, D. Borodin, K. Tamasaku, and S. Shwartz, "Ghost imaging with paired x-ray photons," Phys. Rev. A **97**, 063804 (2018).
16. J. H. Shapiro, "Computational ghost imaging," Phys. Rev. A—Atomic, Mol. Opt. Phys. **78**, 061802 (2008).
17. Y. Bromberg, O. Katz, and Y. Silberberg, "Ghost imaging with a single detector," Phys. Rev. A—Atomic, Mol. Opt. Phys. **79**, 053840 (2009).
18. O. Katz, Y. Bromberg, and Y. Silberberg, "Compressive ghost imaging," Appl. Phys. Lett. **95** (2009).
19. Q.-B. Lu, L. Ding, Y.-Y. Zhou, *et al.*, "Ultrasonic holographic ghost imaging," Phys. Rev. Appl. **17**, 034052 (2022).
20. B. I. Erkmen, "Computational ghost imaging for remote sensing," JOSA A **29**, 782–789 (2012).
21. F. Lin, L. Hong, H. Guo, *et al.*, "Ghost identification for qr codes and fingerprints with thermal light modulation," Phys. Rev. Appl. **18**, 054060 (2022).
22. S. Yuan, D. Chen, X. Liu, and X. Zhou, "Optical encryption based on biometrics and single-pixel imaging with random orthogonal modulation," Opt. Commun. **522**, 128643 (2022).

23. D. V. Strekalov, B. I. Erkmen, and N. Yu, “Ghost imaging of space objects,” in *Journal of Physics: Conference Series,* vol. 414 (IOP Publishing, 2013), p. 012037.
24. A. M. Kingston, D. Pelliccia, A. Rack, *et al.*, “Ghost tomography,” Optica **5**, 1516–1520 (2018).
25. A. M. Kingston, G. R. Myers, D. Pelliccia, *et al.*, “X-ray ghost-tomography: Artefacts, dose distribution, and mask considerations,” IEEE Trans. on Comput. Imaging **5**, 136–149 (2018).
26. H. Zhang, K. Li, F. Wang, *et al.*, “Megapixel x-ray ghost imaging with a binned detector in the object arm,” Chin. Opt. Lett. **20**, 033401 (2022).
27. C.-Z. Zhao, H.-P. Zhang, J. Tang, *et al.*, “X-ray ghost imaging with a specially developed beam splitter,” Synchrotron Radiat. **31** (2024).
28. O. Sefi, A. Ben Yehuda, Y. Klein, *et al.*, “20 μm resolution multipixel ghost imaging with high-energy x-rays,” Opt. Express **32**, 37001–37010 (2024).
29. N. Zhao, J. Tang, C. Zhao, *et al.*, “Synthetic aperture x-ray ghost imaging with sub-micron pixel resolution,” Opt. Express **33**, 972–982 (2025).
30. N. Zhao, J. Tang, C. Zhao, *et al.*, “Parallel ghost imaging with extra large field of view and high pixel resolution,” ChinaXiv (2025).
31. N. Zhao, C. Zhao, J. Tang, *et al.*, “Global ghost imaging,” ChinaXiv (2025).
32. N. Zhao, J. Tang, C. Zhao, *et al.*, “Parallel ghost imaging with ultra low dose and high pixel resolution,” ChinaXiv (2025).
33. N. Zhao, J. Fang, J. Tang, *et al.*, “Generalization of parallel ghost imaging based on laboratory x-ray source,” ChinaXiv (2025).
34. C. Li, W. Yin, H. Jiang, and Y. Zhang, “An efficient augmented lagrangian method with applications to total variation minimization,” Comput. Optim. Appl. **56**, 507–530 (2013).